Colloidal $Cs_{1-x}FA_xPbI_3$ quantum dots derived from ligand-assisted cation exchange for record-efficiency and segregation-free solar cells

Mengmeng Hao[1], Yang Bai[1], Stefan Zeiske[2], Long Ren[3], Junxian Liu[4], Yongbo Yuan[5], Nasim Zarrabi[2], Ningyan Cheng[3], Mehri Ghasemi[1], Peng Chen[1], Shanshan Ding[1], Miaoqiang Lyu[1], Dongxu He[1], Jung Ho Yun[1], Yi Du[3], Yun Wang[4], Ardalan Armin[2], Paul Meredith[2], Gang Liu[6,7], Hui-Ming Cheng[6,8,9], Lianzhou Wang[1]**

[1]Nanomaterials Centre, Australian Institute for Bioengineering and Nanotechnology and School of Chemical Engineering, The University of Queensland, St Lucia, Queensland 4072, Australia.

[2]Department of Physics, Swansea University, Swansea, SA2 8PP, Wales, UK.

[3]Institute for Superconducting and Electronic Materials (ISEM), Australian Institute for Innovative Materials (AIIM), University of Wollongong, Wollongong, New South Wales 2500, Australia.

[4]School of Environment and Science, Centre for Clean Environment and Energy, Griffith University, Gold Coast, Queensland 4222, Australia.

[5]Institute of Super-Microstructure and Ultrafast Process in Advanced Materials, School of Physics and Electronics, Central South University, Changsha, 410083, PR China.

[6]Shenyang National Laboratory for Materials Science, Institute of Metal Research, Chinese Academy of Sciences, 72 Wenhua Road, Shenyang 110016, China

[7]School of Materials Science and Engineering, University of Science and Technology of China, 72 Wenhua Road, Shenyang 110016, China

[8]Shenzhen Geim Graphene Center, Tsinghua-Berkeley Shenzhen Institute (TBSI), Tsinghua University, 1001 Xueyuan Road, Shenzhen 518055, China

[9]Advanced Technology Institute (ATI), University of Surrey, Guildford, Surrey GU2 7XH, UK

* Corresponding authors. Emails: l.wang@uq.edu.au (L.W.); y.bai@uq.edu.au (Y.B.).

Abstract

The mixed caesium and formamidinium lead triiodide perovskite system ($Cs_{1-x}FA_xPbI_3$) in the form of quantum dots (QDs) offers a new pathway towards stable perovskite-based photovoltaics and optoelectronics. However, it remains challenging to synthesize such multinary QDs with desirable properties for high-performance QD solar cells (QDSCs). Here we report an effective ligand-assisted cation exchange strategy that enables controllable synthesis of $Cs_{1-x}FA_xPbI_3$ QDs across the whole composition range (x: 0-1), which is inaccessible in large-grain polycrystalline thin films. The surface ligands play a key role in driving the cross-exchange of cations for the rapid formation of $Cs_{1-x}FA_xPbI_3$ QDs with suppressed defect density. The hero $Cs_{0.5}FA_{0.5}PbI_3$ QDSC achieves a certified record power conversion efficiency (PCE) of 16.6% with negligible hysteresis. We further demonstrate that QD devices exhibit substantially enhanced photostability compared to their thin film counterparts because of the suppressed phase segregation, retaining 94% of the original PCE under continuous 1-sun illumination for 600 hours.

Main

Solution processed organic-inorganic lead halide perovskite materials with a common formulation of ABX_3 (where A is an organic cation or Cs; B is commonly Pb or Sn; and X is a halide) have shown promise in many applications including photovoltaics (PVs)[1, 2, 3, 4], light-emitting diodes (LEDs)[5, 6], and lasers[7, 8]. This potential is in part due to a range of desirable optoelectronic properties, such as large absorption coefficient, long carrier diffusion length and low exciton dissociation energy. The rapidly increasing power conversion efficiencies (PCEs) for perovskite solar cells (PSCs), which have been achieved with mixed methylammonium (MA) and formamidinium (FA) A-site cations and mixed Br and I X-site anions, have matched or surpassed other more established technologies such as multicrystalline silicon, cadmium telluride (CdTe) and copper indium gallium selenide (CIGS) photovoltaics [9, 10, 11]. However, device degradation due to MA degassing and photoinduced halide segregation remains a critical hurdle for commercialization[12, 13, 14]. $Cs_{1-x}FA_xPbI_3$ without Br and volatile MA was recently demonstrated as a promising perovskite formulation, showing enhanced moisture-, thermal-, and photo-stability[12, 13, 14]. Unfortunately, solar cells using $Cs_{1-x}FA_xPbI_3$ perovskites suffer from large open-circuit voltage (V_{OC}) losses despite rubidium (Rb) or polymer passivation[12, 14, 15], and thus their PCEs still lag behind those of the state-of-the-art perovskites containing MA and Br. Furthermore, it is still challenging to continuously tune the

compositions of $Cs_xFA_{1-x}PbI_3$ at room temperature[16], and a considerably high percentage ($x \geq 0.15$) of Cs incorporation can cause cation segregation under continuous light illumination or with an applied bias[13, 17]. This hinders optical bandgap optimization and long-term operational stability for tandems and colour-tuning of LEDs[13, 18, 19].

A promising approach towards the mitigation of these challenges lies in the synthesis of perovskites in the form of nanometre-sized quantum dots (QDs) or nanocrystals. Perovskite QDs have shown notable advantages over their large-grain perovskite thin film (often called bulk) counterparts. These advantages include: additional bandgap-tuning by utilising the quantum-confinement effect[20]; multi-exciton generation (MEG)[21]; near-unity photoluminescence quantum yield (PLQY)[20, 22]; and photon up- and down-conversion [23, 24]. Thus, QDs offer great promise to surpass the Shockley-Queisser limit[25] and further boost the efficiency of tandem devices. Another advantage of perovskite QDs is the colloidal synthesis and processability using industrially friendly solvents at room temperature, which decouples grain crystallization from film deposition and enables rapid low-cost manufacturing [26]. More importantly, both colloidal $CsPbI_3$ and $FAPbI_3$ QDs exhibit significantly enhanced phase stability at room temperature[26, 27] in comparison with their bulk counterparts, providing a new strategy for improving the lifetime of PSCs. Perovskite QDs that are defect-tolerant have shown great promise over traditional chalcogenide QDs when incorporated into PV devices[20]. $CsPbI_3$ QD solar cells (QDSC) have delivered a larger open-circuit voltage (V_{OC})[26, 28] than thin-film counterparts yielding a certified PCE of 13.4%[29], which breaks the record efficiency of PbS QDSCs. However, both $CsPbI_3$ and $FAPbI_3$ QDs are highly susceptible to moisture and polar solvents during post-synthesis purification and surface treatment[26, 27, 30, 31]. This poses significant challenges in effective ligand engineering and causes a significant increase in surface defects, which limits the carrier transport and thus PCE enhancement.

Mixed-cation $Cs_{1-x}FA_xPbI_3$ QDs are more desirable than pure $CsPbI_3$ and $FAPbI_3$ QDs in terms of stability and charge transport properties. This is believed to be due to the concomitant incorporation of FA and Cs inducing entropic stabilization of the perovskite structure under ambient condition[16], and the fast rotation of FA resulting in enhanced orbital overlap and easier polaron formation that lead to longer carrier lifetimes and reduced non-radiative recombination[32, 33]. Unfortunately, the rational synthesis of such multinary QDs with desirable optoelectronic properties remains a significant challenge considering the complex interplay between the bulk thermodynamics of the solid solutions, crystal surface energies, and dynamics of capping ligands in solution[34, 35]. Hence, only a few studies have been reported so far (e.g.,

droplet-based microfluidics, cation exchange) to explore the synthesis of $Cs_{1-x}FA_xPbI_3$ QDs[34, 35, 36, 37], but their use as a single light absorbing layer in QDSCs resulted in deteriorated PCEs[36] and the PCEs of state-of-the-art QDSCs[38] still lag far behind that of the respective thin film counterparts.

Here we report a ligand-assisted cation exchange strategy to synthesize high-quality $Cs_{1-x}FA_xPbI_3$ QDs + in a time- and cost-efficient manner. We show that the surface ligands are important for the formation and diffusion of A-site cation vacancies, which play a critical role in driving the cross-exchange of cations. Compared to pure $CsPbI_3$ or $FAPbI_3$ QDs, the resultant $Cs_{1-x}FA_xPbI_3$ QDs are far more stable in ambient air or polar solvents and exhibit significantly lower trap density and longer carrier lifetime. Solar cells fabricated with colloidal $Cs_{0.5}FA_{0.5}PbI_3$ QDs under ambient conditions deliver a certified steady-state PCE of 16.6%, a new record for the QDSC category [11]. We also find a larger PLQY of 10% and thus reduced non-radiative recombination in perovskite QD devices relative to their bulk counterparts, which explains the smaller V_{OC} losses observed in perovskite QDSCs. We further demonstrate that the use of colloidal $Cs_xFA_{1-x}PbI_3$ QDs opens a new avenue towards segregation-free PSCs showing enhanced stability under continuous light illumination beyond the reach of large-grain perovskite thin films of identical compositions.

Ligand-assisted synthesis of $Cs_{1-x}FA_xPbI_3$ QDs

We first calculated the energies (ΔE_{ex}) required for the formation of $Cs_{1-x}FA_xPbI_3$ (x=0.25, 0.50 and 0.75) (Supplementary Fig. 1) via A-site cation exchange, and the negative values suggest that this reaction is thermodynamically favourable. To prepare the alloy $Cs_{1-x}FA_xPbI_3$ QDs, $CsPbI_3$ and $FAPbI_3$ QDs were first synthesized using a modified hot-injection method and then mixed in controlled molar ratios. We took the synthesis of $Cs_{0.5}FA_{0.5}PbI_3$ QDs as an example to explore the feasibility and closely monitored the A-site cation exchange reaction between the parent $CsPbI_3$ and $FAPbI_3$ QDs. When the parent colloidal solutions were purified twice with methyl acetate before mixing, a large fraction of OA ligands were removed as indicated by the significant reduction of the vibration bands at 1640 cm^{-1} (–C=C– group) in the Fourier-Transform Infrared (FTIR) spectra (Supplementary Fig. 2), forming an OA-less environment. The cation exchange reaction was very slow, taking more than 24 hours as shown in **Figure 1A** and the as-prepared alloy sample was denoted as QD-OL. The slow reaction is in accordance with a previous report[36], which indicates the presence of a high kinetic barriers for the cations to leave the starting QDs and diffuse into other QDs. We proposed that the OA ligands could be the key to eliminating such barriers by solvating A-site cations of QDs as

highly mobile Cs-oleate and FA-oleate in the colloidal solution. To examine this hypothesis, we intentionally kept more OA ligands in the parent colloidal solutions by reducing the purification to once, forming an OA-rich environment. Encouragingly, we observed a rapid completion (30 min) of the cation exchange reaction (**Fig. 1B**). We also observed a rapid cation exchange reaction (colour change) by adding Cs-oleate in $FAPbI_3$ QD solution or adding FA-oleate in $CsPbI_3$ QD solution as shown in Supplementary Fig. 3, while adding other salts such as caesium (formamidinium) acetate and caesium (formamidinium) iodide did not lead to cation exchange, which suggests the critical role of OA in solvating A-site cations of QDs and validates the existence of mobile Cs-oleate and FA-oleate reaching an equilibrium in the colloidal solution. The ligand density in each colloidal QD solution was estimated and summarized in Supplementary Table 1. The as-synthesized alloy sample in the OA-rich environment was named as QD-OR. Part of this sample was purified again and denoted as QD*-OR. Interestingly, we note that the alloy QDs synthesized in the OA-rich environment showed much higher PL intensity (**Fig. 1C**) and the corresponding PLQYs (Supplementary Fig. 4) are 2-3 times higher than that prepared in the OA-less environment. We further checked the influence of different solvents on the cation exchange reaction. Supplementary Fig. 5 shows the evolution of the PL emission peaks with time for both solvents (toluene and octane), which both exhibit rapid cation exchange comparable to that in hexane. These results verify our hypothesis that the noteworthy difference in ligand engineering is the key, which not only promotes the cation exchange reaction, but also preserves high radiative efficiency by suppressing the formation of surface defects as illustrated in the scheme (**Fig. 1D**).

By using this ligand-assisted cation exchange method, we demonstrate the fine-tuning of the absorption onset and PL emission peak (Supplementary Fig. 6) of the alloy QDs from pure $CsPbI_3$ to pure $FAPbI_3$. The bandgaps of each QD composition are summarized in Supplementary Table 2. All the alloy $Cs_{1-x}FA_xPbI_3$ QDs retain their perovskite structure, as shown in the XRD patterns (Supplementary Fig. 7a). The zoomed-in view of the XRD patterns (Supplementary Fig. 7b) indicates that the substitution of Cs^+ with FA^+ induces a gradual shift in the diffraction peaks such as (200) towards a lower angle.

Scanning transmission electron microscopy (STEM) images (Supplementary Fig. 8a-e) reveal that all the $Cs_{1-x}FA_xPbI_3$ QDs are uniform nanocubes with size around 14 ± 2 nm. To identify the distribution of Cs and FA cations and understand the structural evolution in atomic resolution among these samples, high angle annular dark-field STEM (HAADF-STEM) characterizations were conducted, as shown in Supplementary Fig. 8f-j. The $CsPbI_3$ QDs in

Supplementary Fig. 8f show a perfect cubic perovskite structure along the [001] zone axis with Pb−I atom columns exhibiting higher contrast and Cs and I atom columns showing weaker contrast (brightened-and-dimmed contrast distributions). However, for the alloy QDs containing FA, the atomic contrast distribution in the HAADF-STEM images is different, showing some regions with uniform atomic contrast distribution instead of brightened-and-dimmed contrast distribution. The HAADF-STEM image of $FAPbI_3$ QD (Supplementary Fig. 8j) shows uniform contrast distribution for nearly all atom columns, and the atomic arrangements match very well with hexagonal PbI_2 along $[\bar{4}41]$ direction with a lattice parameter of approximately 3.2 Å[39], which we assume is due to the e-beam induced decomposition. To reveal the original crystal structure of alloy QDs, $Cs_{0.5}FA_{0.5}PbI_3$ QD (**Figure 2 A, B**) was selected as a model for structural analysis. As shown in **Fig. 2C** and **D**, the observed atomic column arrangements could be regarded as the mixture of $CsPbI_3$ along the [001] direction and PbI_2 along the $[\bar{4}41]$ direction, and the area ratio between them (based on the colour coded image, **Fig. 2D**) is about 1:1, consistent with the molar ratio of Cs and FA in this sample. Along the [001] direction, an atomic model (**Fig. 2F**) was established from the zoomed-in view (**Fig. 2E**) for the region marked with a red square in the experimental HAADF-STEM image. The simulated atomic resolution HAADF-STEM image (**Fig. 2G**) via QSTEM software further confirmed the consistency between the model and the sample structure along this direction. Therefore, in the atomic resolution HAADF-STEM images of the alloy QDs, the regions matching PbI_2 along the $[\bar{4}41]$ direction with uniform atomic contrast distribution can be assigned to the original $FAPbI_3$ along the [001] direction. The other regions with brightened-and-dimmed contrast distribution can be assigned to the $CsPbI_3$ along the [001] direction. To confirm this, we established another model along the [110] direction of the $Cs_{0.5}FA_{0.5}PbI_3$ QD for structural analysis (Supplementary Fig. 9). Based on the models from these two directions, we restored the $FAPbI_3$ structure at the position of the PbI_2 observed in experimental images. The simulated atomic resolution HAADF-STEM image and the atomic models of the as-synthesized $Cs_{0.5}FA_{0.5}PbI_3$ QD along the [001] zone axis are shown in **Fig. 2H** and **Fig. 2I**, respectively. Thus it is reasonable to state that FA and Cs involved in the cation-exchange reaction were distributed among the corner-sharing PbI_6 octahedrons and grew into small $FAPbI_3$ and $CsPbI_3$ units, which assembled randomly in three dimensions to form a single cubic-shape alloy $Cs_{1-x}FA_xPbI_3$ QDs (**Fig. 2J**).

QD device architecture and certified efficiency

To confirm the critical role of ligand concentration in determining the quality of mixed-cation QDs, we first fabricated a batch of QDSCs using $Cs_{0.5}FA_{0.5}PbI_3$ QDs prepared in OA-rich environment (C_2F_2-Q-OR), $Cs_{0.5}FA_{0.5}PbI_3$ QDs prepared in OA–less environment (C_2F_2-Q-OL) and pure $CsPbI_3$ QDs as the control sample (C-Q). The device configuration is shown in the scheme (Supplementary Fig. 10). **Figure 3A** presents a transmission electron microscopy (TEM) cross-section image of a typical QDSC. As shown in the typical *J-V* curves (**Fig. 3B**), the control (C-Q) device had a short-circuit current density (J_{SC}) of 15.4 mA cm^{-2}, a V_{OC} of 1.16 V and a fill factor (FF) of 53.9%, yielding a PCE of 9.6%. Unexpectedly, the C_2F_2-Q-OL device delivered a lower J_{SC} of 14.6 mA cm^{-2} and V_{OC} of 1.08 V, resulting in a PCE of 10.1% comparable to that of control device. In clear contrast, a distinctly enhanced J_{SC} of 18.4 mA cm^{-2} and FF of 77.9% were achieved in the C_2F_2-Q-OR device, which boosted the PCE over 16%. Detailed photovoltaic device parameters including the average values can be found in Supplementary Table 3.

Colloidal $Cs_{1-x}FA_xPbI_3$ QDs of different stoichiometry derived from OA-rich condition were then incorporated into QDSCs to further investigate the impact of FA incorporation. Large-grain $Cs_{1-x}FA_xPbI_3$ bulk thin film solar cells with the same device structure were also fabricated for comparison and the Cs fraction was up to 0.25 only because of the previously mentioned difficulty in achieving stable compositions with higher ratios of Cs[16]. Supplementary Fig. 11 shows the photocurrent density-voltage (*J-V*) characteristics of QDSCs with different compositions and bulk $Cs_{0.25}FA_{0.75}PbI_3$ devices. The typical *J-V* curves obtained on both reverse and forward scans for each QD composition are shown in Supplementary Fig. 12. Compared to $CsPbI_3$ and $FAPbI_3$ QD devices, all the alloy $Cs_{1-x}FA_xPbI_3$ QD devices showed negligible photocurrent hysteresis. Unlike the previous report[36], we observed that all the devices fabricated with alloy $Cs_{1-x}FA_xPbI_3$ QDs exhibited markedly increased PCEs compared to those with pure $CsPbI_3$ QDs, as summarized in **Fig. 3C**. All these PCEs were obtained on the reverse scan. The enhanced PCE of alloy $Cs_{1-x}FA_xPbI_3$ QD devices relative to the pure $CsPbI_3$ QD devices is due to the improvement in J_{SC} and FF as well as the reduction in V_{OC} loss (**Fig. 3C**). The $Cs_{0.5}FA_{0.5}PbI_3$ QDSCs delivered the best photovoltaic performance with the average PCE increased from ~10 to 15% upon FA incorporation. A hero device fabricated with $Cs_{0.5}FA_{0.5}PbI_3$ QD was sent to an accredited laboratory (Newport, USA) for certification. **Fig. 3D** is the *J-V* curve of the hero device without encapsulation measured under a 10 point IV sweep configuration wherein the bias voltage (current for V_{OC} determination) is held constant until the measured current (voltage for V_{OC}) is determined to be unchanging. This is intended

to represent the quasi-steady-state performance of the device. The hero device delivered a certified efficiency of 16.6% with a V_{OC} of 1.17 V, a J_{SC} of 18.3 mA cm^{-2}, and a FF of 78.3% (Supplementary Fig. 13-14), which is currently the highest certified efficiency of colloidal QDSCs reported to date[11]. It is noted that no anti-reflection coating was applied in this champion device. No obvious photocurrent hysteresis was observed in this device (tested at the Newport labs, USA) and additional three devices tested in our lab by changing the voltage-sweep direction (Supplementary Fig. 15 and Fig. 16). The integrated J_{SC} from external quantum efficiency (EQE) spectrum measured at Newport reached 17.9 mA cm^{-2} as shown in **Fig. 3E**, which is in good agreement with that from *J–V* measurement. In addition, we note that all QD devices exhibited much higher V_{OC} than those of large-grain bulk $Cs_{0.25}FA_{0.75}PbI_3$ devices (**Fig. 3B**) as well as other bulk $Cs_{1-x}FA_xPbI_3$ devices reported in the literature[12, 14, 15].

Synergistic effect of ligand and FA on defect reduction

All mixed-cation $Cs_{1-x}FA_xPbI_3$ QDs derived from OA-rich environment have delivered significantly higher PV performance compared to that of pure $CsPbI_3$ QDSCs, which we tentatively ascribe to their enhanced light harvesting because of the smaller bandgap and reduced trap density. The broader spectral absorption with FA incorporation (Supplementary Fig. 6a) is apparently the key reason for the improved light harvesting, resulting in higher J_{SC}. However, deteriorated J_{SC} and V_{OC} were observed in the device with $Cs_{0.5}FA_{0.5}PbI_3$ QDs prepared under OA-less condition and the overall PCE was comparable to that of $CsPbI_3$ QD devices. To find the origin of such distinct difference, we first performed time-resolved PL (TRPL) decay measurements on various QD thin films. As shown in **Fig. 3F**, a much longer carrier lifetime of 97 ns was deduced from the fitted TRPL decay curve of the C_2F_2-Q-OR film, which was more than three times longer than that (26 ns) of the control C-Q film. This is consistent with previous studies showing that the incorporation of FA cation leads to longer carrier lifetime and reduced non-radiative recombination[32, 33]. However, no obvious lifetime increase was observed for the C_2F_2-Q-OL film with relative to the C-Q sample. We speculate that this is because the insufficient coverage of surface ligands on the parent $CsPbI_3$ and $FAPbI_3$ QDs could easily generate additional defects either before or during the cation exchange reaction given their vulnerable nature in polar solvent and ambient air. STEM analysis was performed on $Cs_{0.5}FA_{0.5}PbI_3$ QDs obtained in both OA-rich and OA-less conditions, and we indeed observed more defect sites on the QDs obtained in the OA-less condition as shown in the atomic-resolution HAADF-STEM images (Supplementary Fig. 17). Therefore, the prolonged charge recombination lifetime observed in C_2F_2-Q-OR sample should be ascribed to

the synergistic effect of ligand and FA in suppressing the formation of deep-trap defects that cause non-radiative trap-assisted recombination. To confirm the defect reduction, we then performed the space charge–limited current (SCLC) measurements. The hole-only devices were fabricated using different QDs (C_2F_2-Q-OR, C_2F_2-Q-OL, and C-Q), and their current-voltage curves are shown in **Fig. 3G**. In all cases a linear (Ohmic) rise at lower voltages was observed followed by a logarithmic slope greater than 3 as the voltage increases. This is indicative of trap-filling, and the cross-over voltage (V_{TFL}) between the two slopes is often taken as the trap filling voltage from which the trap density can at least be estimated. While this approach is quite robust for single crystals (which are electrically thick), we would caution that the trap-filling voltage is subject to considerable uncertainty in thin film diodes because of the finite shunt resistance due to the inevitable defects and pin holes which impact the initial Ohmic part of the current rise. However, what can be seen from these measurements is that the trap filling occurs in relative terms at lower voltages in the C_2F_2-Q-OR device versus the C-Q and C_2F_2-Q-OL devices indicating lower trap density, which leads to significant FF improvement and smaller V_{OC} loss in the corresponding QDSCs. Again, this indicates that a ligand-rich environment is essential to achieving significant defect reduction by FA incorporation. To further understand the mechanism of FA-induced deep-trap defect reduction, we calculated the formation energy of two typical defects, iodide interstitial (I_i) and lead vacancy (V_{Pb}) as a proof-of-concept. I_i and V_{Pb} have been demonstrated to be the most important deep-trap defects in perovskite materials that are mainly responsible for the charge recombination processes[40, 41]. The optimized defect structures of I_i and V_{Pb} on the $Cs_{1-x}FA_xPbI_3$ are shown in Supplementary Figs. 18-19. **Fig. 3H** summarizes the formation energy of I_i (ΔE_{I_i}) and V_{Pb} ($\Delta E_{V_{Pb}}$) for different compositions and $Cs_{0.5}FA_{0.5}PbI_3$ shows the highest formation energy for both types of defects. The positive values reveal that the defect formation in all compositions is an endothermic process. Compared to $CsPbI_3$ and $FAPbI_3$, the higher formation energy explains why it is more difficult to form I_i and V_{Pb} deep-trap defects in the $Cs_{1-x}FA_xPbI_3$ (x=0.25, 0.50 and 0.75, respectively) perovskites, and this is qualitatively consistent with the experimental results.

Mechanistic study of V_{OC} loss in QD devices

The more optimal V_{OC} deficit observed in QD devices relative to bulk devices led us to consider what is unique about perovskite QDs in suppressing V_{OC} loss. To uncover the origin, we first performed a detailed balance analysis. The V_{OC} of a solar cell can be written in terms of

radiative ($\Delta V_{OC,R}$), non-radiative ($\Delta V_{\mathrm{OC,BNR}}$) and surface recombination ($\Delta V_{\mathrm{OC,SR}}$) losses relative to the bandgap:

$$V_{OC} = E_g/q \ - \Delta V_{\mathrm{OC,R}} - \Delta V_{\mathrm{OC,BNR}} - \Delta V_{\mathrm{OC,SR}} \quad (1)$$

We note that surface recombination (which can be thought of as extraction of carriers by the "wrong" contact) is also a non-radiative process. As such, we must distinguish it from bulk non-radiative recombination (for example Shockley-Read-Hall) in order to explain the V_{OC} improvements that we observe. The non-radiative loss here is a bulk property and labelled with the subscript (BNR) to emphasize that it does not include surface recombination so that $\Delta V_{\mathrm{OC,NR}} = \Delta V_{\mathrm{OC,BNR}} + \Delta V_{\mathrm{OC,SR}}$. $\Delta V_{OC,SR}$ is defined by the difference between the quasi-Fermi level splitting ($\mu = E_{fn} - E_{fp}$) in the bulk of the semiconductor and contacts:

$$q\Delta V_{\mathrm{OC,SR}} = \mu_{\mathrm{bulk}} - \mu_{\mathrm{conact}} = \mu_{\mathrm{bulk}} - qV_{\mathrm{OC}} \quad (2)$$

Quasi-Fermi level splitting in the bulk can be imagined as a V_{OC} in the absence of surface recombination leading to the well-known relation: $\mu_{\mathrm{bulk}} = kT\ln(\frac{Jsc}{j_0})$ derived from the Shockley equation where j_0 is the dark saturation current excluding surface recombination contribution. Using the well-established relation between PLQY and radiative and total dark saturation current ($j_0 = j_{0,R}/\mathrm{PLQY}$) we can write $\mu_{\mathrm{bulk}} = kT\ln(\mathrm{PLQY}\frac{Jsc}{j_{0,R}})$, while the radiative limit of V_{oc} is $V_{\mathrm{oc},R} = \frac{kT}{q}\ln(\frac{Jsc}{j_{0,R}})$. $j_{0,R}$ is the radiative saturation dark current, which is calculated from integrating the product of the black body flux and external quantum efficiency measured sensitively to include the sub-bandgap states (Supplementary Fig. 20). This approach has recently been applied to perovskite thin film solar cells[42]. The non-radiative open circuit loss (excluding non-radiative surface recombination) is also determined from the PLQY so that $\Delta V_{OC,NR} = \frac{kT}{q}\ln(\mathrm{PLQY}^{-1})$. To undertake this analysis, we measured the PLQY of full devices under open circuit conditions and monochromatic (520 nm) irradiance equivalent to 1 sun. A small AC perturbation was superimposed on the pump light whose modulation was used to detect the PL signal with a high degree of sensitivity using a spectrum analyzer. The advantage of measuring PLQY of the full device under open circuit and operational illumination conditions is that the emission efficiency is measured at carrier (and indeed ion) concentrations and profiles relevant to operational open circuit. Furthermore, PLQY is related to the quasi-Fermi level splitting of the bulk, thus the results are not affected by the surface recombination.

The values of V_{OC}, μ_{bulk}, $j_{0,R}$, $\Delta V_{OC,NR}$ and $\Delta V_{OC,SR}$ for the bulk and QD devices derived from this analysis are given in Supplementary Table 4. For QD devices, PLQY values as large as 10% were obtained (at one sun-equivalent), meaning reduced non-radiative losses versus the bulk perovskite cells. Likewise, **Figure 4A** shows the voltage loss due to the surface recombination and non-radiative recombination in bulk and QD devices: $\Delta V_{OC,NR}$ decreased from 150 meV to 60 meV with 30 meV reduction in $\Delta V_{OC,SR}$. We attribute the reduction in the surface recombination to the reduced trap density of the QD devices lowering the surface recombination velocity induced by mid-gap trap states near the contact. Similar values are observed for $x = 0.5$. This data also indicates that the V_{OC} of these QDSCs can be improved by contact engineering to further reduce the surface recombination. By making perfectly selective contacts, the V_{OC} can in principle be improved to 1.2 V which is only 70 meV lower than the ultimate radiative limit (see supplementary Table 4).

In a deeper analysis (**Fig. 4B** and **C**), light intensity dependent V_{OC} measurements over a large dynamic range reveal that recombination in both $Cs_{0.25}FA_{0.75}PbI_3$ bulk (C_1F_3-B) and QD (C_1F_3-Q) devices is trap-assisted-dominated with ideality factors close to 2. By increasing the light intensity, we observe the bulk device remains trap-limited (ideality factor nearly 2), whereas the V_{OC} in the QD device increases sharply (with an ideality factor of 4 within an intermediary intensity range) before reaching a new regime with ideality factor of 1 (band-to-band recombination-dominated). Preliminary PL results also suggest that PLQY increases with the background light intensity in the QD devices. From both results it can be concluded that the recombination is predominantly trap-assisted in both bulk and QD devices at low light intensities, whereas at high light intensities band-to-band recombination in the QD devices is dominant hence the larger PLQY and ideality factor of 1. This distinct property might be the key origin of the reduced V_{OC} loss observed in QD devices.

Note that the exact reason of the ideality factor of 4 in the intermediary V_{OC} range is not entirely clear. We have repeatedly observed it in the intermediate range in all QD devices at different measurement frequencies and scan rates, which is an interesting observation worthy of further investigation.

Stability of $Cs_{1-x}FA_xPbI_3$ QD thin films and devices

We then evaluated the stability of alloy $Cs_{1-x}FA_xPbI_3$ QDs under ambient conditions. The PCE evolutions of both $CsPbI_3$ and $Cs_{0.5}FA_{0.5}PbI_3$ QDSCs without encapsulation were monitored over a long storage time scale, which were periodically measured in ambient with a relative

humidity of 50-70%. As shown in Supplementary Fig. 21, the performance of the $CsPbI_3$ QD device degraded rapidly and lost the majority of its efficiency within four days. In strong contrast, the efficiency of the $Cs_{0.5}FA_{0.5}PbI_3$ QD device retained over 97% of its original efficiency after storage for 20 days.

It is generally accepted that the formation and migration of ionic defects within the halide perovskite lattice are potential sources of intrinsic instability for perovskite photovoltaics[18, 43]. As discussed above, significant reduction of surface defects was demonstrated for alloy $Cs_{1-x}FA_xPbI_3$ QD films, which we consider would contribute to the enhancement of operational stability of the corresponding device. To exclude other factors such as Spiro-OMeTAD that is vulnerable under thermal stress, we first checked the stability of QD thin films by monitoring the PL emission change before and after continuous light irradiation in an N_2 atmosphere. For easy comparison, we fabricated a $Cs_{0.25}FA_{0.75}PbI_3$ QD thin film and a bulk perovskite thin film of identical composition. The QD film showed a significant blue shift in the PL peak position compared to the bulk film, indicating the quantum confinement retained in the QD film. Under continuous illumination for 96 hours, the PL emission peak had a red shift of 12 nm in the bulk $Cs_{0.25}FA_{0.75}PbI_3$ thin film (**Figure 5A**). The photoinduced change to the emission of bulk perovskite films originates from light-induced cation migration and segregation, which could lead to device burn-in and accelerate the degradation of PSCs operated in an inert atmosphere[18]. Encouragingly, we found that the $Cs_{0.25}FA_{0.75}PbI_3$ QD film exhibited negligible change in PL emission (**Fig. 5B**) after being illuminated for the same period of time, suggesting the suppressed ion migration in QD films. To confirm this, we performed an ion conductivity measurement on lateral devices fabricated with $Cs_{0.25}FA_{0.75}PbI_3$ bulk and QD thin films. As shown in **Fig. 5C**, the activation energy for ion migration in bulk $Cs_{0.25}FA_{0.75}PbI_3$ film drops from 0.54 eV to 0.34 eV, indicating a reduced energy barrier for ions to move after illumination. However, the activation energy for ion migration in QD samples does not change (**Fig. 5D**) after illumination, which suggests that light irradiation does not intensify ion migration in QD films. This is consistent with recent studies showing that lowering the diffusion length tends to decrease the rate of segregation, and both theoretical and experimental results indicate a segregation-free region for perovskites with a certain grain size below a threshold of 46 ± 7 nm[44, 45]. The remaining capping ligands that passivate the surface of QDs may also contribute to the reduction of defect-mediated ion migration.

We further examined the long-term stability of QD devices under light. Completed devices without encapsulation were held at open-circuit under continuous 1-sun illumination without

cooling (the device temperature was measured to be *ca.* 50-65 °C) in N_2, which could help exclude other environmental factors that affect the device performance. As a reference, the $Cs_{0.25}FA_{0.75}PbI_3$ bulk device quickly lost over 20% of its initial efficiency under the same conditions (**Fig. 5E**). In sharp contrast, the $Cs_{0.25}FA_{0.75}PbI_3$ and $Cs_{0.5}FA_{0.5}PbI_3$ QDSCs retained 90% and 94% of their original PCEs after 600 hours (**Fig. 5E**) because of the coupled long-term V_{OC} and FF stability (Supplementary Fig. 22), respectively. The enhanced long-term stability in the QDSCs relative to the bulk devices can be ascribed to the enhanced phase stability of QD films under continuous light illumination, which we believe is closely related to the suppressed ion migration within QD films as discussed above. We anticipate the efficiency and operational stability of QDSCs could be further improved with more stable hole transport materials and appropriate interface engineering. Our demonstration of the exceptional long-term stability of perovskite QDSCs sheds light on a new direction to address the intrinsic stability issue of perovskite PVs and optoelectronics.

Conclusion

In summary, we have developed an effective ligand-assisted cation exchange strategy that enables controllable synthesis of mixed-cation $Cs_{1-x}FA_xPbI_3$ QDs with remarkable ambient stability. We show that the surface ligands play a key role in driving the cross-exchange of cations for the formation of $Cs_{1-x}FA_xPbI_3$ QDs featuring reduced defect density and improved carrier mobility. Solar cells fabricated with $Cs_{1-x}FA_xPbI_3$ QDs exhibit reduced voltage losses compared to $CsPbI_3$ QDs and corresponding bulk perovskite cells, yielding a certified record PCE of 16.6% for QDSCs. The suppressed phase segregation in $Cs_{1-x}FA_xPbI_3$ QDs accounts for the superior photostability of QDSCs over their bulk counterpart devices. We anticipate that colloidal $Cs_{1-x}FA_xPbI_3$ QDs will offer a new and promising avenue for fabricating efficient and stable flexible devices, tandem solar cells and a range of optoelectronics such as LEDs, photodetectors and lasers.

Methods

Chemicals

All chemicals were purchased from Sigma Aldrich and used without purification, unless otherwise noted. Cesium carbonate (Cs_2CO_3, 99.9%), lead (II) iodide (PbI_2 99.9985%, Alfa Aesar), oleic acid (OA, technical grade 90%), oleylamine (OLA, technical grade 70%), 1-octadecene (ODE, technical grade 90%), toluene (anhydrous 99.8%), hexane (reagent grade ≥95%), octane (anhydrous, ≥99%), methyl acetate (MeOAc, anhydrous 99.5%), ethyl acetate

(EtOAc, anhydrous 99.5%), lead (II) acetate trihydrate ($Pb(OAc)_2 \cdot 3H_2O$, 99.999%), formamidine acetic acid salt (≥99%), oleylamonium iodide (OLA-I, ≥99%, Xi'an Baolaite) (lead (II) nitrate ($Pb(NO_3)_2$, 99.999%), rhodamine-6G (99%), ethanol (EtOH, Merk, ≥99.5%), SnO_2 nanoparticle dispersion (15% in H_2O, Alfa Aesar), (2,2',7,7'-Tetrakis(N,N-di-p-methoxyphenylamine)-9,9-spirobifluorene (spiro-OMeTAD, ≥99.5%, Xi'an Baolaite), chlorobenzene (anhydrous, 99.8%), 4-tert-butylpyridine (96%, Aldrich), bis(trifluoromethane)sulfonimide lithium salt (Li-TFSI), and acetonitrile (anhydrous, 99.8%).

Synthesis of colloidal $Cs_{1-x}FA_xPbI_3$ QDs

$CsPbI_3$ QDs were synthesized following the previous report[46] with some modification. Cs-oleate was obtained by dissolving 0.1 g Cs_2CO_3 into 0.4 mL OA and 10 mL ODE, the mixture were loaded into a 50 mL 3-neck flask and stirred under vacuum for 30 min at 120 °C. After fully dissolving, the Cs-oleate in ODE was stored in N_2 until it was used. PbI_2 (0.4 g), ODE (20 mL), OA (2 mL) and OLA (2 mL) were stirred in a 100 mL flask and degassed under vacuum at 120 °C for one hour. The flask was then filled with N_2 and kept under constant N_2 flow. The temperature was increased to 170°C, then 3.2 mL of the Cs-oleate (~0.063 M) precursor was swiftly injected into the mixture. After 5-10 s, the reaction was quenched by immediate immersion of the flask into an ice bath. After cooling to room temperature, 30 mL MeOAc were added, and the mixture was centrifuged at 8000 rpm for 5 min. The resulting QD-precipitate was dispersed in hexane with a concentration of 50 mg/ml and stored under nitrogen until use.

$FAPbI_3$ QDs were synthesized following the previous report[34]. $Pb(acetate)_2 \cdot 3H_2O$ (0.152 g), FA-acetate (0.157 g), ODE (16 mL), and OA (4 mL) were added in a 25 mL three-neck flask and dried under vacuum for 30 min at 40 °C. The mixture was then heated to 80 °C under N_2 atmosphere, followed by the injection of OLA-I (0.474 g dissolved in 4 mL of toluene). After 30 s, the reaction mixture was cooled in the water bath. After cooling to room temperature, 20 mL MeOAc were added, and the mixture was centrifuged at 8000 rpm for 5 min. The resulting QD-precipitate was dispersed in hexane with a concentration of 50 mg/mL and stored under nitrogen for further use.

For the cation exchange reactions conducted in a ligand rich environment, the stored $CsPbI_3$ and $FAPbI_3$ QDs were purified once with MeOAc. Their molar concentrations were determined before mixing in controlled ratios. The ligand-assisted cation exchange reaction was completed in 30-60 min at room temperature. We note that this ligand-assisted cation-exchange technique

is versatile and very efficient, which could be easily integrated with those high-volume QD manufacturing platforms such as continuous-flow microfluidic reactor without adding significant cost. The resultant mixed-cation QDs were purified by adding EtOAc (volume ratio of QDs solution to EtOAc is 1:2) and centrifuged at 8000 rpm for 5 min. This process was repeated once more to further purify the QDs. Finally, octane was added to disperse the QDs with concentration around 60mg/ml for solar cell fabrication. For the cation exchange reactions conducted in the ligand less environment, the stored $CsPbI_3$ and $FAPbI_3$ QDs were purified twice with MeOAc before mixing and the reaction took over 48 h.

Device fabrication

SnO_2 layer: Glass/indium doped tin oxide (ITO) substrates were cleaned with successive sonication in 2-propanol, acetone and 2-propanol each for 15 min, respectively. The cleaned substrates were further treated in an ultraviolet-ozone chamber before use. The SnO_2 colloidal solution (Alfa Aesar) was diluted by H_2O to 1.5% and spin coated onto glass/ITO substrates at 3000 rpm for 30 s, and then baked on a hot plate in air at 150 °C for 30 min.

QD films: First, saturated $Pb(NO_3)_2$ in MeOAc solution and FAI in EtOAc solution were prepared. For thin film fabrication process, the QDs (~60 mg/mL in octane) were spin-coated on SnO_2 substrate at 2000 RPM for 30 sec, and then swiftly dipped in the $Pb(NO_3)_2$ solution. The saturated $Pb(NO_3)_2$ solution was used to maintain the surface structure of QDs by alleviating the dissolving of lead atoms from QDs during the removal of long-chain ligands. The film was rinsed using neat, anhydrous MeOAc, and then dried with a stream of air. This procedure was repeated four times. The films were then soaked in the FAI solution for 10 s to enhance the electronic coupling, which was followed by MeOAc rinsing and drying[29]. Deposition of all QD films was performed in air (relative humidity, < 40%).

Bulk $Cs_xFA_{1-x}PbI_3$ films: To prepare $Cs_xFA_{1-x}PbI_3$ precursor solution with excess lead iodide, FAI (1 M) and PbI_2 (1.1 M) were dissolved in a mixed solvent of DMF and DMSO (1:4 v/v), followed by adding CsI stock solution (1.5 M in DMSO) to achieve the desired composition. The perovskite precursor was spin-coated on SnO_2 substrates at 2000 rpm for 10 s and 6000 rpm for 30 s, in which 200 μL of CB was dropped on the spinning substrate 15 s prior to the end of second step. The substrates were then annealed on hot plate at 65 °C for 10 min and 100 °C for 60 min to obtain crystalline perovskite films.

HTM and electrode: The spiro-OMeTAD solution was prepared by dissolving 73.5 mg of spiro-OMeTAD in 1 mL of chlorobenzene, then 28.8 μl of 4-tert-butylpyridine and 17.5 μl of

Li-TFSI (520 mg/mL in acetonitrile) solution was added. The spiro-OMeTAD solution was spin-coated onto the QD/bulk perovskite films at 4000 rpm for 30 s. Gold electrode was then deposited by thermally evaporation at 0.5 Å /s for a total thickness of 80 nm.

Characterization

UV-Vis absorption spectra for colloidal solutions were collected using a Jasco V670 spectrometer in transmission mode. Powder X-ray diffraction (XRD) patterns were obtained with a STOE STADI P powder diffractometer. A germanium monochromator, Cu Kα1 irradiation and a silicon strip detector (Dectris Mythen) were used. The functional groups of the films were characterized by an FTIR spectrometer (Nicolet 5700 FTIR) with an ATR accessory. The steady-state PL emissions from QD solutions and films were measured at 450 nm light source excitation using a monochromatized Xe lamp, and the time-resolved PL decay studies were carried out with a 377 nm pulsed diode laser excitation source on a fluorescence spectrophotometer (FLSP-900, Edinburgh Instruments). The PLQYs of QD solutions were estimated according to standard procedure using rhodamine 6G as a reference dye [47].

STEM examination was carried out using a probe-corrected JEOL ARM200F equipped with a cold field emission gun operating at an acceleration voltage of 200 kV. HAADF images were acquired with inner and outer collection angles of 68 and 280 mrad, respectively, ensuring Z-contrast, while bright field images were acquired with a maximum collection angle of 17 mrad. All images (1024 × 1024 pixels) were acquired with a 10 ms per pixel dwell time and convergence angle of 25 mrad, resulting in a probe size about 0.1 nm and a current of 26.4 pA. Images were processed by the Gatan Digital Micrograph software follow the steps below: Spatial filter was used to smooth the image first, and then we combine the FFT filter with the mask tool to get rid of the noise. We also used the deconvolution tool to increase the quality of the images. QSTEM software was used to simulate the HAADF-STEM images of $Cs_{0.5}FA_{0.5}PbI_3$ along the different zone axis. The input parameters were set according to the experimental conditions. Probe size, convergence angle and acceptance angle of the ADF detector are critical and accounted for in the image simulation.

The cross-section lamellae of solar cell device was prepared with a Scios DualBeam focused ion beam-scanning electron microscope (FEI, Oregon, USA) system. Images were obtained with a FEI F20 FEG-S/TEM instrument.

Space-charge-limited current I-V measurements (SCLC) was performed on devices with structure of ITO/PEDOT:PSS/QDs/spiro-OMeTAD/Au. For device fabrication, PEDOT:PSS

solution was filtered through 0.45μm PTFE filter and spin-coated onto ITO at 4000 rpm for 60 s. Afterwards, the film was baked on a hot plate in air at 150 °C for 30 min. The other layers was fabricated using the same procedure as in solar cell device fabrication. Current as a function of the applied voltage was measured using IVIUMnSTAT in the dark. A non-linear response was observed and analysed according to SCLC theory[48].

The *J-V* curves were measured with a source meter (Keithley 2420) using a solar simulator (Newport, Oriel Class AAA, 94063A) at 100 mW/cm^2 illumination (AM 1.5 G) equipped with a calibrated silicon reference cell and meter (Newport, 91150V) certificated by the National Renewable Energy Laboratory (NREL). The *J-V* curves were measured in reverse scan (from 1.3 V to -0.1 V) and forward scan (from -0.1 V to 1.3 V) modes at a scan speed of 100 mV/s with a delay time of 100 ms. There was no preconditioning before measurement. A metal shadow mask (0.058 cm^2) was used to define the active area of devices and all devices were measured in ambient air. For long-term light stability, the unsealed devices were illuminated under continuous 100 mW cm^{-2} irradiation by a LED grow light (Spectrum King MLH140) under open-circuit condition in N_2 atmosphere.

Lateral devices with a configuration of ITO/Bulk perovskite or QD film/Au were fabricated for ion conductivity measurements. The QD films were prepared following the same procedure as that for QDSC fabrication. The ion conductivity (σ) was extracted from the current changes of a lateral device under 0.35 V/μm electrical field, the activation energy for ion migration was obtained by fitting the ion conductivity at different temperatures according to the Arrhenius equation [49].

Light intensity dependent photovoltage: For light intensity dependent open-circuit voltage (V_{oc}) measurements, the voltage at an applied device current of $I = 0$ A (open-circuit) was measured at an illumination wavelength of 520 nm (Oxxius laser diode) as a function of light irradiance. Prior to light coupling into an integrating sphere (Thorlabs, IS236A-4), two combined filter wheels containing different optical density (OD) filters attenuated the light irradiance over a dynamic range of 70 dB. The integrating sphere was used to simultaneously record the V_{OC} using a source-meter unit (Keithley 2450) and to record the incident light irradiance with a Silicon photodiode sensor (Thorlabs, SM05PD1A). For the light irradiance calibration, a Thorlabs NIST-calibrated Silicon photodiode sensor (S121C) was used.

Solar cell PLQY measurements: A background CW light was used to bring the solar cell to 1-sun equivalent condition at which V_{OC} and J_{SC} are approximately equal to those determined at

AM1.5G condition. The wavelength of the laser was 520 nm (Oxxius laser diode). A small perturbation (less than 1% of the CW background light) was imposed to the background light at a modulation frequency of 7 Hz. Integrated photoluminescence was measured using a silicon photodetector (SM1PD1B) and a long-pass filters at 550nm and 650 nm to eliminate the scattered pump. Photodetector signal was pre-amplified using a Femto DHPCA-100 at a gain of 10^7 V/A. Photodetector signal was then recorded using a Spectrum Analyser (Keysight N9010A) at a resolution bandwidth of 1 Hz. The PL signal was at least 40 dB larger than the electrical noise floor and stray pump laser. The photodetector current was then converted to the photon flux received at the photodetector position. The total flux emitted by the device was calculated based upon a nearly Lambertian emission and photodetector flux. The PLQY was determined from the total flux and the intensity of the modulated pump. During the measurement, the solar cell was under open circuit condition.

REFERENCES AND NOTES

1. Kojima A, Teshima K, Shirai Y, Miyasaka T. Organometal Halide Perovskites as Visible-Light Sensitizers for Photovoltaic Cells. *J. Am. Chem. Soc.* **131**, 6050-6051 (2009).

2. Kim H-S, *et al.* Lead Iodide Perovskite Sensitized All-Solid-State Submicron Thin Film Mesoscopic Solar Cell with Efficiency Exceeding 9%. *Sci. Rep.* **2**, 591 (2012).

3. Lee MM, Teuscher J, Miyasaka T, Murakami TN, Snaith HJ. Efficient Hybrid Solar Cells Based on Meso-Superstructured Organometal Halide Perovskites. *Science* **338**, 643-647 (2012).

4. Burschka J, *et al.* Sequential deposition as a route to high-performance perovskite-sensitized solar cells. *Nature* **499**, 316-319 (2013).

5. Lin K, *et al.* Perovskite light-emitting diodes with external quantum efficiency exceeding 20 per cent. *Nature* **562**, 245-248 (2018).

6. Cao Y, *et al.* Perovskite light-emitting diodes based on spontaneously formed submicrometre-scale structures. *Nature* **562**, 249-253 (2018).

7. Xing G, *et al.* Low-temperature solution-processed wavelength-tunable perovskites for lasing. *Nat. Mater.* **13**, 476-480 (2014).

8. Zhu H, *et al.* Lead halide perovskite nanowire lasers with low lasing thresholds and high quality factors. *Nat. Mater.* **14**, 636 (2015).

9. Jeon NJ, *et al.* Compositional engineering of perovskite materials for high-performance solar cells. *Nature* **517**, 476-480 (2015).

10. Jiang Q, *et al.* Surface passivation of perovskite film for efficient solar cells. *Nat. Photon.*, (2019).

11. https://www.nrel.gov/pv/cell-efficiency.html.

12. Lee J-W, Kim D-H, Kim H-S, Seo S-W, Cho SM, Park N-G. Formamidinium and Cesium Hybridization for Photo- and Moisture-Stable Perovskite Solar Cell. *Adv. Energy Mater.* **5**, 1501310 (2015).

13. Huang J, Xu P, Liu J, You X-Z. Sequential Introduction of Cations Deriving Large-Grain $Cs_xFA_{1-x}PbI_3$ Thin Film for Planar Hybrid Solar Cells: Insight into Phase-Segregation and Thermal-Healing Behavior. *Small* **13**, 1603225 (2017).

14. Turren-Cruz S-H, Hagfeldt A, Saliba M. Methylammonium-free, high-performance, and stable perovskite solar cells on a planar architecture. *Science* **362**, 449-453 (2018).

15. Saliba M, *et al.* Incorporation of rubidium cations into perovskite solar cells improves photovoltaic performance. *Science* **354**, 206-209 (2016).

16. Li Z, Yang M, Park J-S, Wei S-H, Berry JJ, Zhu K. Stabilizing Perovskite Structures by Tuning Tolerance Factor: Formation of Formamidinium and Cesium Lead Iodide Solid-State Alloys. *Chem. Mater.* **28**, 284-292 (2016).

17. Kubicki DJ, Prochowicz D, Hofstetter A, Zakeeruddin SM, Grätzel M, Emsley L. Phase Segregation in Potassium-Doped Lead Halide Perovskites from 39K Solid-State NMR at 21.1 T. *J. Am. Chem. Soc.* **140**, 7232-7238 (2018).

18. Domanski K, *et al.* Migration of cations induces reversible performance losses over day/night cycling in perovskite solar cells. *Energy Environ. Sci.* **10**, 604-613 (2017).

19. Christians JA, *et al.* Tailored interfaces of unencapsulated perovskite solar cells for >1,000 hour operational stability. *Nat. Energy* **3**, 68-74 (2018).

20. Akkerman QA, Rainò G, Kovalenko MV, Manna L. Genesis, challenges and opportunities for colloidal lead halide perovskite nanocrystals. *Nat. Mater.*, (2018).

21. Li M, *et al.* Low threshold and efficient multiple exciton generation in halide perovskite nanocrystals. *Nat. Commun.* **9**, 4197 (2018).

22. Pan J, *et al.* Bidentate Ligand-Passivated $CsPbI_3$ Perovskite Nanocrystals for Stable Near-Unity Photoluminescence Quantum Yield and Efficient Red Light-Emitting Diodes. *J. Am. Chem. Soc.* **140**, 562-565 (2018).

23. Zheng W, *et al.* Near-infrared-triggered photon upconversion tuning in all-inorganic cesium lead halide perovskite quantum dots. *Nat. Commun.* **9**, 3462 (2018).

24. Zhou D, *et al.* Cerium and Ytterbium Codoped Halide Perovskite Quantum Dots: A Novel and Efficient Downconverter for Improving the Performance of Silicon Solar Cells. *Adv. Mater.* **29**, 1704149 (2017).

25. Shockley W, Queisser HJ. Detailed Balance Limit of Efficiency of p-n Junction Solar Cells. *J. Appl. Phys.* **32**, 510-519 (1961).

26. Swarnkar A, *et al.* Quantum dot–induced phase stabilization of α-$CsPbI_3$ perovskite for high-efficiency photovoltaics. *Science* **354**, 92-95 (2016).

27. Xue J, *et al.* Surface Ligand Management for Stable $FAPbI_3$ Perovskite Quantum Dot Solar Cells. *Joule* **2**, 1866-1878 (2018).

28. Yuan J, *et al.* Band-Aligned Polymeric Hole Transport Materials for Extremely Low Energy Loss α-$CsPbI_3$ Perovskite Nanocrystal Solar Cells. *Joule* **2**, 2450-2463 (2018).

29. Sanehira EM, *et al.* Enhanced mobility $CsPbI_3$ quantum dot arrays for record-efficiency, high-voltage photovoltaic cells. *Sci. Adv.* **3**, (2017).

30. Wheeler LM, *et al.* Targeted Ligand-Exchange Chemistry on Cesium Lead Halide Perovskite Quantum Dots for High-Efficiency Photovoltaics. *J. Am. Chem. Soc.* **140**, 10504-10513 (2018).

31. Lin J, *et al.* Thermochromic halide perovskite solar cells. *Nat. Mater.* **17**, 261-267 (2018).

32. Kubicki DJ, *et al.* Cation Dynamics in Mixed-Cation $(MA)_x(FA)_{1-x}PbI_3$ Hybrid Perovskites from Solid-State NMR. *J. Am. Chem. Soc.* **139**, 10055-10061 (2017).

33. Zhu H, *et al.* Screening in crystalline liquids protects energetic carriers in hybrid perovskites. *Science* **353**, 1409-1413 (2016).

34. Protesescu L, *et al.* Dismantling the "Red Wall" of Colloidal Perovskites: Highly Luminescent Formamidinium and Formamidinium–Cesium Lead Iodide Nanocrystals. *ACS Nano* **11**, 3119-3134 (2017).

35. Lignos I, *et al.* Exploration of Near-Infrared-Emissive Colloidal Multinary Lead Halide Perovskite Nanocrystals Using an Automated Microfluidic Platform. *ACS Nano* **12**, 5504-5517 (2018).

36. Hazarika A, *et al.* Perovskite Quantum Dot Photovoltaic Materials beyond the Reach of Thin Films: Full-Range Tuning of A-Site Cation Composition. *ACS Nano* **12**, 10327-10337 (2018).

37. Suri M, *et al.* Enhanced Open-Circuit Voltage of Wide-Bandgap Perovskite Photovoltaics by Using Alloyed (FA1–xCsx)Pb(I1–xBrx)3 Quantum Dots. *ACS Energy Lett.* **4**, 1954-1960 (2019).

38. Zhao Q, *et al.* High efficiency perovskite quantum dot solar cells with charge separating heterostructure. *Nat. Commun.* **10**, 2842 (2019).

39. Chen S, *et al.* Atomic scale insights into structure instability and decomposition pathway of methylammonium lead iodide perovskite. *Nat. Commun.* **9**, 4807 (2018).

40. Meggiolaro D, *et al.* Iodine chemistry determines the defect tolerance of lead-halide perovskites. *Energy Environ. Sci.* **11**, 702-713 (2018).

41. Meggiolaro D, De Angelis F. First-Principles Modeling of Defects in Lead Halide Perovskites: Best Practices and Open Issues. *ACS Energy Lett.* **3**, 2206-2222 (2018).

42. Stolterfoht M, *et al.* The impact of energy alignment and interfacial recombination on the internal and external open-circuit voltage of perovskite solar cells. *Energy Environ. Sci.* **12**, 2778-2788 (2019).

43. Boyd CC, Cheacharoen R, Leijtens T, McGehee MD. Understanding Degradation Mechanisms and Improving Stability of Perovskite Photovoltaics. *Chem. Rev.* **119**, 3418-3451 (2019).

44. Draguta S, *et al.* Rationalizing the light-induced phase separation of mixed halide organic–inorganic perovskites. *Nat. Commun.* **8**, 200 (2017).

45. Gualdrón-Reyes AF, *et al.* Controlling the Phase Segregation in Mixed Halide Perovskites through Nanocrystal Size. *ACS Energy Lett.* **4**, 54-62 (2019).

46. Protesescu L, *et al.* Nanocrystals of Cesium Lead Halide Perovskites ($CsPbX_3$, X = Cl, Br, and I): Novel Optoelectronic Materials Showing Bright Emission with Wide Color Gamut. *Nano Lett.* **15**, 3692-3696 (2015).

47. Grabolle M, Spieles M, Lesnyak V, Gaponik N, Eychmüller A, Resch-Genger U. Determination of the Fluorescence Quantum Yield of Quantum Dots: Suitable Procedures and Achievable Uncertainties. *Anal. Chem.* **81**, 6285-6294 (2009).

48. Shi D, *et al.* Low trap-state density and long carrier diffusion in organolead trihalide perovskite single crystals. *Science* **347**, 519-522 (2015).

49. Mizusaki J, Arai K, Fueki K. Ionic conduction of the perovskite-type halides. *Solid State Ion.* **11**, 203-211 (1983).

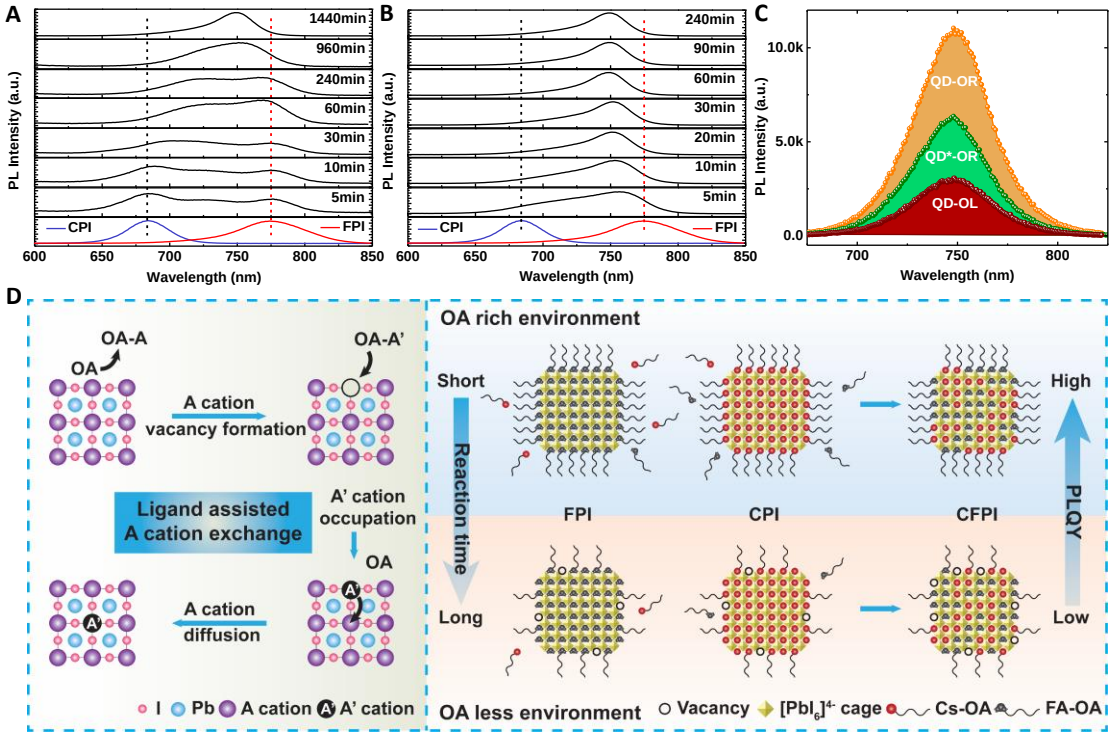

Figure 1. **Mechanism of ligand-assisted A-site cation exchange reaction. (A, B)** The evolution of PL emission peaks with time to form $Cs_{0.5}FA_{0.5}PbI_3$ QDs by combining parent QD solutions that were purified twice (OA-less) and once (OA-rich), respectively. The bottom-most spectra in these two figures show the individual PL emissions from $CsPbI_3$ (CPI, in blue) and $FAPbI_3$ (FPI, in red). The remaining emission spectra are shown for the temporal evolution with time. Prior to mixing, they exhibit a photoluminescence (PL) peak at 683 nm and 774 nm. In the OA-less environment, after mixing at room temperature, the two distinct peaks did not move substantially from the original positions of $CsPbI_3$ and $FAPbI_3$ QDs at least up to 30 min. Investigations of the intermediate stages of this process indicate that exchange occurs simultaneously in both kinds of QDs; the $CsPbI_3$ PL peaks shift to longer wavelengths and the $FAPbI_3$ PL moves to shorter wavelengths. It then took tens of hour for the two peaks to merge into one single broad peak. Subsequently, the complete composition homogenization was achieved in another eight hours. In the OA-rich environment, the two PL peaks immediately merge into one upon mixing and the resulting emission spectrum stopped changing in around 30 min, which indicates the extremely rapid completion of cation exchange. **(C)** PL spectra of QD-OL, QD-OR, and QD*-OR in hexane. QD-OL: as-synthesized $Cs_{0.5}FA_{0.5}PbI_3$ QDs in OA-less environment; QD-OR: as-synthesized $Cs_{0.5}FA_{0.5}PbI_3$ QDs in OA-rich environment; QD*-OR: QD-OR purified once. (**D**) Schematic illustration of the proposed A-site cation exchange reaction mechanism. OA: oleic acid; CPI: $CsPbI_3$; FPI: $FAPbI_3$; CFPI: $Cs_{1-x}FA_xPbI_3$. Desorption of solvated cations from QDs leaves behind cation vacancies at the surface for the new cations to occupy. Shuttling of FA^+ and Cs^+ cations between QDs will be facilitated by the diffusion of Cs-oleate and FA-oleate in the solution. In OA-rich solution, the formation and diffusion of solvated A-site cations will be promoted, leading to facilitated cation exchange; while insufficient OA ligand would result in much less solvated A^+ cations that can diffuse in the non-polar solvent, which limits the cation cross-exchange between the parent QDs.

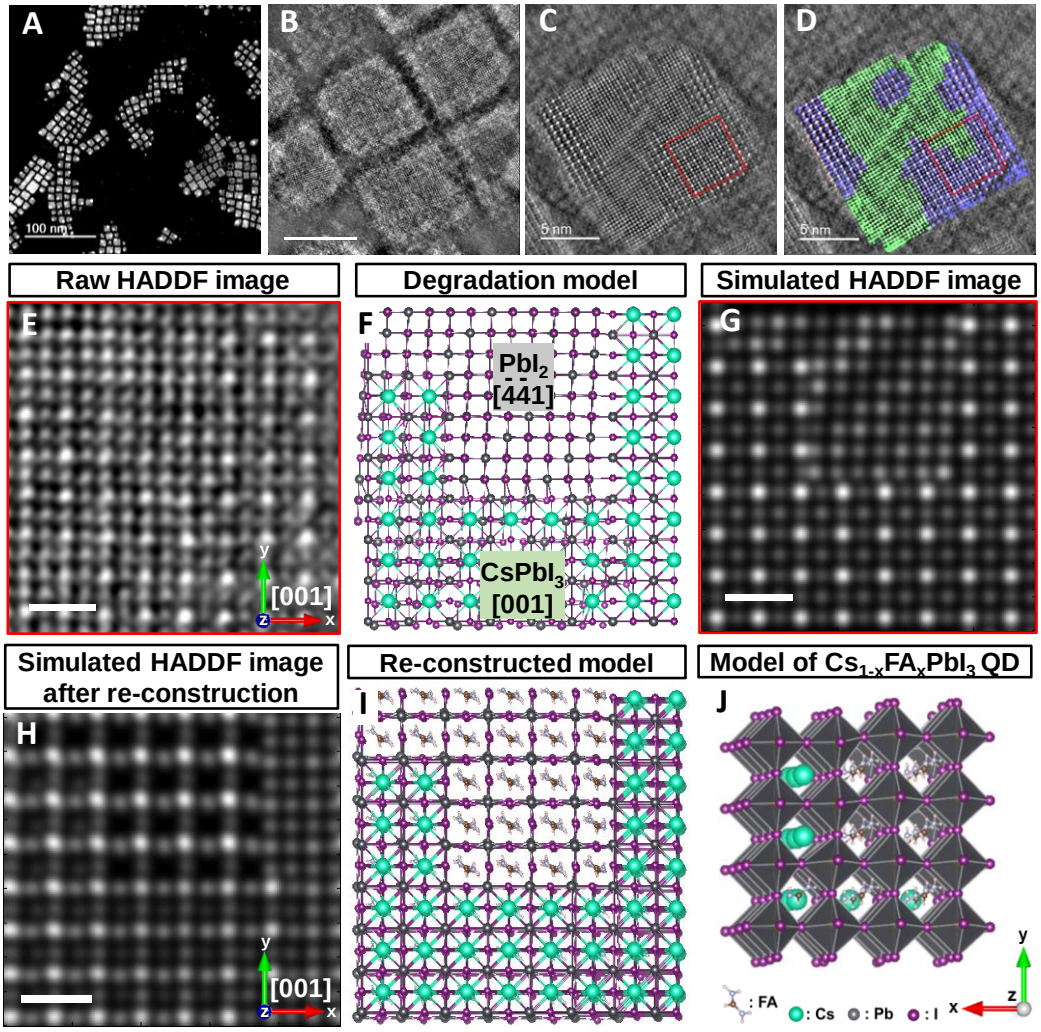

Figure 2. **Morphology and crystal structure of $Cs_{1-x}FA_xPbI_3$ QD**. (**A, B**) HAADF-STEM images of $Cs_{0.5}FA_{0.5}PbI_3$ QDs. (**C, D**) Representative atomic-resolution HAADF-STEM image and the derived color-coded image of $Cs_{0.5}FA_{0.5}PbI_3$ QD. The image is viewed along the cubic [001] zone axis established from the lattice arrangement similar with the original $CsPbI_3$ (or $FAPbI_3$) cubic crystal structure; the green dots represent the atom column in the area that are uniform contrast distribution, the red dots and purple dots (red color represent the high contrast atoms and purple color represent the low contrast atoms) represent the atom columns in the area that are distinct contrast distribution. (**E**) The zoom-in view, (**F**) the atomic models, and (**G**) the simulated atomic resolution HAADF-STEM image for the region marked with a red square. All the experimental STEM images of the samples containing FA are distorted due to the fast decomposition of local crystal structure from $FAPbI_3$ to PbI_2 under e-beam illumination. (**H**) The simulated atomic resolution HAADF-STEM image and (**I**) the atomic models for the original view of $Cs_{0.5}FA_{0.5}PbI_3$ QD along the [001] zone axis after re-construction. (**J**) The established crystal structure of the $Cs_{1-x}FA_xPbI_3$ QD. Scale bar in **E**, **G**, **H**, 10 Å.

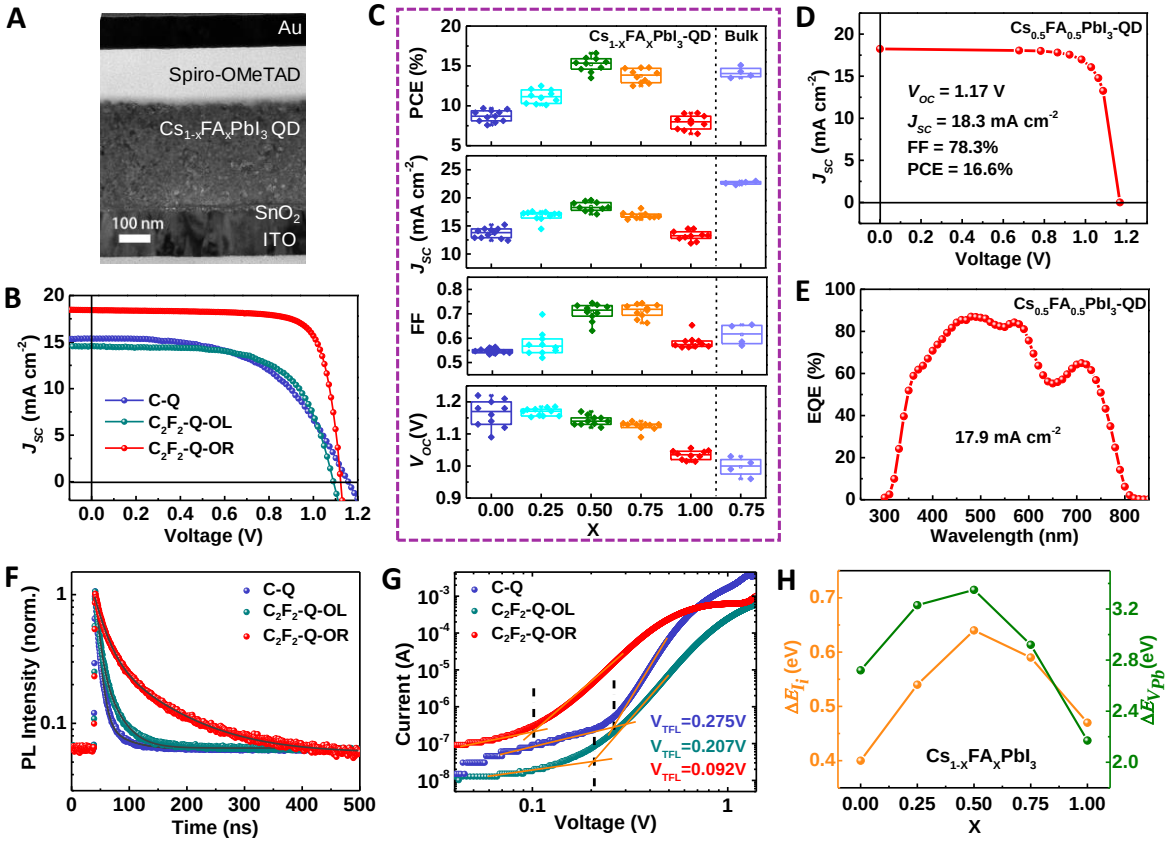

Figure 3. **Photovoltaic performance and optoelectronic characteristics of QD thin films and devices.** (**A**) Cross-section TEM image of the $Cs_{1-x}FA_xPbI_3$ QDSC. (**B**) Typical *J-V* curves of QDSCs using different QDs. C-Q: $CsPbI_3$ QDs; C_2F_2-Q-OL: $Cs_{0.5}FA_{0.5}PbI_3$ QDs derived in OA–less environment; C_2F_2-Q-OR: $Cs_{0.5}FA_{0.5}PbI_3$ QDs derived in OA-rich environment. (**C**) Performance evolution (PCE, J_{SC}, FF, and V_{OC}) of solar cells based on $Cs_{1-x}FA_xPbI_3$ QDs of different compositions (11 devices for each composition) and bulk $Cs_{0.25}FA_{0.75}PbI_3$ (5 devices). Mixed-cation QDs were prepared in OA-rich environment. (**D**) Certificated *J-V* curve and (**E**) EQE spectrum of the hero device measured at Newport PV Lab, USA; the integrated J_{SC} is indicated. (**F**) Time-resolved photoluminescence (TRPL) spectra of C-Q, C_2F_2-Q-OL, and C_2F_2-Q-OR thin films on glass substrates. (**G**) *J-V* characteristics of hole-only devices (ITO/PEDOT:PSS/QD/Spiro-OMeTAD/Au), used for estimating the SCLC defect concentration of C-Q, C_2F_2-Q-OL, and C_2F_2-Q-OR samples. (**H**) Formation energy of I_i (ΔE_{I_i}) and V_{Pb} ($\Delta E_{V_{Pb}}$) of $Cs_{1-x}FA_xPbI_3$ with different x values.

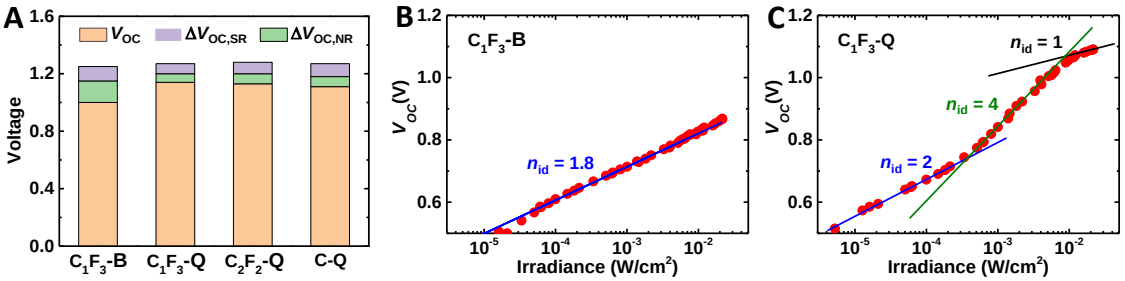

Figure 4. ***V*$_{OC}$ loss mechanism in QD device**. (**A**) Voltage loss due to the surface recombination and non-radiative recombination in bulk and QD devices. Light intensity dependent V_{OC} measurements over a large dynamic range in C_1F_3-B device (**B**) and C_1F_3-Q device (**C**). C_1F_3-B: bulk $Cs_{0.25}FA_{0.75}PbI_3$; C-Q: $CsPbI_3$ QDs; C_1F_3-Q: $Cs_{0.25}FA_{0.75}PbI_3$ QDs; C_2F_2-Q: $Cs_{0.5}FA_{0.5}PbI_3$ QDs. Mixed-cation QDs were derived in OA-rich environment.

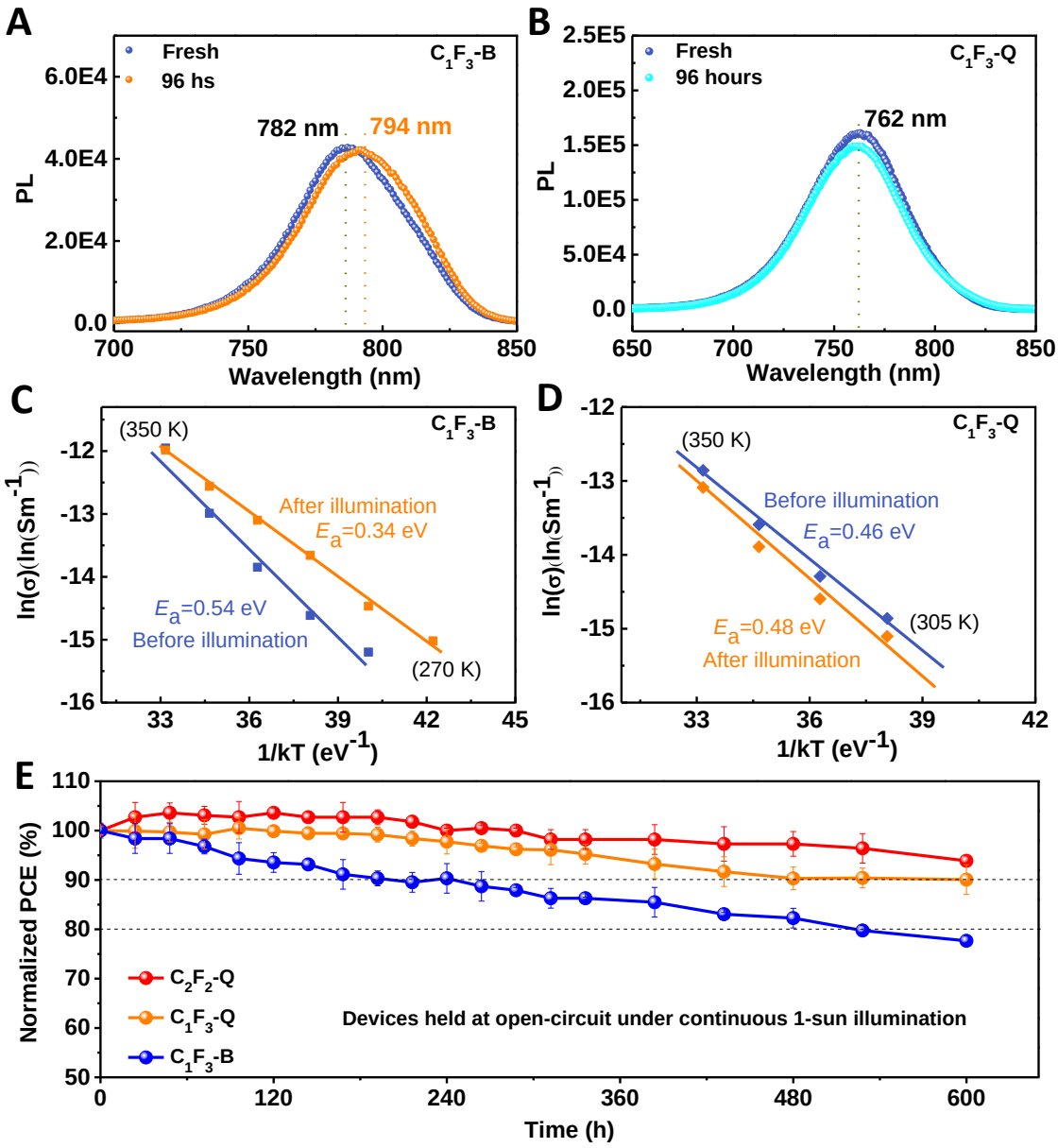

Figure 5. **Stability of QD thin film and devices.** PL spectra of C_1F_3-B film (**A**) and C_1F_3-Q film (**B**) on SnO_2-coated ITO substrates before and after illumination for 96 hours in N_2, respectively. Arrhenius plot of the ion conductivity of C_1F_3-B film (**C**) and C_1F_3-Q film (**D**) before and after illumination (25 mW cm^{-2}) for 3 hours, respectively, from the slope of which the activation energy for ion migration is calculated. (**E**) Long-term stability of unencapsulated solar cells fabricated with C_1F_3-B film, C_1F_3-Q film, and C_2F_2-Q film monitored at open-circuit under 1-sun illumination in N_2 atmosphere. C_1F_3-B: bulk $Cs_{0.25}FA_{0.75}PbI_3$; C_1F_3-Q: $Cs_{0.25}FA_{0.75}PbI_3$ QDs; C_2F_2-Q: $Cs_{0.5}FA_{0.5}PbI_3$ QDs. Mixed-cation QDs were derived in OA-rich environment.

ACKNOWLEDGMENTS

Funding: The financial support from the Australian Research Council Discovery Projects (ARC DPs) are highly appreciated. Y.B. acknowledges the support from UQ Development Fellowship and ARC DECRA Fellowship (DE190101351). The authors acknowledge the facilities and the scientific support from the Queensland node of the Australian National Fabrication Facility and Australian Microscopy & Microanalysis Research Facility at the Centre for Microscopy and Microanalysis, The University of Queensland. The authors also acknowledge the use of the facilities at the University of Wollongong Electron Microscopy Centre funded by ARC grants (LE0882813 and LE120100104). Y.D. acknowledges the financial support from the ARC (DP160102627, DP170101467, and FT180100585). All computations were undertaken on the supercomputers in National Computational Infrastructure (NCI) in Canberra, Australia, which is supported by the Australian Commonwealth Government, and Pawsey Supercomputing Centre in Perth with the funding from the Australian government and the Government of Western Australia. P.M. is a Sêr Cymru II National Research Chair and A.A. a Sêr Cymru II Rising Star Fellow. The work at Swansea University was funded through the Sêr Cymru II (Welsh European Funding Office and European Regional Development Fund) Program 'Sustainable Advanced Materials'.

Author contributions: Y.B., M.H. and L.W. conceived the project. L.W. and Y.B. supervised the work. M.H. synthesized the perovskite quantum dot (QD) materials, fabricated and characterized the QD thin films and devices with the assistance of S.D.. Y.B. designed the experiments of understanding ligand-assisted cation exchange reaction mechanism and the role of surface ligands. S.Z., N.Z., A.A. and P.M. conducted the electrical and photophysical characterization of QD devices. L.R., N.C. and Y.D. performed STEM study and analysis. J.L. and Y.W. conducted DFT calculations. M.G. and M.L. performed the cross-sectional TEM characterisation. Y.Y. conducted the ion conductivity measurement. P.C. and D.H. fabricated perovskite thin films and devices. Y.B. drafted the manuscript with the help from M.H., A.A., L.R., and J.L.. L.W., P.M., G.L. and H.C. revised the manuscript. All the authors discussed the results and commented on the manuscript.

Competing financial interests: The authors declare no competing financial interests.

Data availability: The data that support the findings of this study are available from the corresponding authors upon reasonable request.